npj | quantum materials

www.nature.com/npjquantmats

ARTICLE OPEN

Check for updates

Transport measurement of fractional charges in topological models

Shu-guang Cheng[1], Yijia Wu[2,3], Hua Jiang[3,4]✉, Qing-Feng Sun[2,5] and X. C. Xie[2,3,6]

The static topological fractional charge (TFC) in condensed matter systems is related to the band topology and thus has potential applications in topological quantum computation. However, the experimental measurement of these TFCs in electronic systems is quite challenging. We propose an electronic transport measurement scheme in which both the charge amount and the spatial distribution of the TFC can be extracted from the differential conductance through a quantum dot coupled to the topological system being measured. For one-dimensional Su–Schrieffer–Heeger (SSH) model, both the $e/2$ charge of the TFC and its distribution can be verified. As for the disorder effect, it is shown that the Anderson disorder, which breaks certain symmetry related to the TFC, is significant in higher-dimensional systems while having little effect on the one-dimensional SSH chain. Nonetheless, our measurement scheme can still work well for specific higher-order topological insulator materials, for instance, the $2e/3$ TFC in the breathing kagome model could be confirmed even in the presence of disorder effect. These conclusions about spatial dimension and disorder effect are quite universal, which also applies to other topological systems such as topological classic wave system.

npj Quantum Materials (2023)8:30; https://doi.org/10.1038/s41535-023-00558-7

INTRODUCTION

The fractional charge, widely existing in a variety of topological systems, directly relates to the non-trivial topology of electronic states and is of great significance in the field of condensed matter physics[1–9]. There are mainly two categories of fractional charge: the moving type and the static type. The former kind acts as charge carrier in the fractional quantum Hall (FQH) states[1–4]. And the later one, can be found as topological edge states in many topological materials, such as one-dimensional systems with the Jackiw-Rebbi mechanism[5–9], topological crystalline insulators with disclination[10], and higher-order topological insulators[11–17]. Remarkably, both the moving[18–21] and the static fractional charges[22–26] follow the quantum statistics beyond the Boson/Fermion statistics and can be employed for topological quantum computation.

Back in 1997, the moving fractional charge in the FQH state was experimentally verified via the transport measurement of shot noise[27,28]. The detection of the static topological fractional charge (TFC), in contrast, is quite challenging in condensed matter systems. The direct measurement of TFC via scanning tunneling spectroscopy is hindered by the experimental resolution[29]. In addition to that, earlier theories have proposed an approach to detect the Jackiw-Rebbi zero mode through its π-period Aharanov–Bohm oscillation[22,30]. Although the presence of the zero mode could be certificated, the charge amount of the static TFC cannot be determined in such a proposal. In another earlier theoretical work[31], a proposal is raised based on an effective model where the TFC trapped by the magnetic domains can be detected via the Coulomb blockade. Such a simplified scheme, in which the entire electronic structure as well as the disorder effect are excluded, has not been confirmed in a more realistic lattice model. Another drawback of this scheme is that the spatial distribution of the TFC cannot be obtained. It is worth noting that although the experimental measurement of TFC has recently been reported in classical wave systems[29,32–34], the elusive disorder effect remains to be further investigated. Significantly, the TFC state here is occupied only when an input with certain frequency is provided. The absence of Fermi surface hinders the verification of the quantum statistics of the TFC in classical wave systems.

In recent years, remarkable progresses for the experimental realization of Su–Schrieffer–Heeger (SSH) model in condensed matter systems have been made by engineering graphene nanoribbons[35–38]. By precisely decorating the graphene nanoribbon edge profiles, both the topologically trivial and non-trivial states are manifested through scanning tunneling spectroscopy. Owing to these progress, the enthusiasm for the discrimination and measurement of TFC in topological materials has been highly raised.

In this theoretic work, the static TFC in topological systems is obtained through the electronic transport of a quantum dot (QD) coupled to the topological system. For the SSH model, both the $e/2$ TFC and its spatial distribution is obtained from transport results. The disorder effect, which is widely presented in topological systems supporting TFC but has not been thoroughly studied yet, is also intensively investigated in this work. The Anderson disorder breaking certain symmetry related to the TFC generally has significant effect on the TFC. However, such effect is greatly suppressed in one-dimensional system that for disordered SSH chain, the TFC amount measured is still in good agreement with the clean result. For certain higher-order topological materials, e.g. some armchair-edged breathing kagome material, the well-localized TFC possessing $2e/3$ charge could also be confirmed by our transport scheme even under disorder.

[1]Department of Physics, Northwest University, Xi'an, China. [2]International Center for Quantum Materials, School of Physics, Peking University, Beijing, China. [3]Institute for Nanoelectronic Devices and Quantum Computing, Fudan University, Shanghai, China. [4]Institute for Advanced Study, Soochow University, Suzhou, China. [5]CAS Center for Excellence in Topological Quantum Computation, University of Chinese Academy of Sciences, Beijing, China. [6]Hefei National Laboratory, Hefei, China.
✉email: jianghuaphy@suda.edu.cn

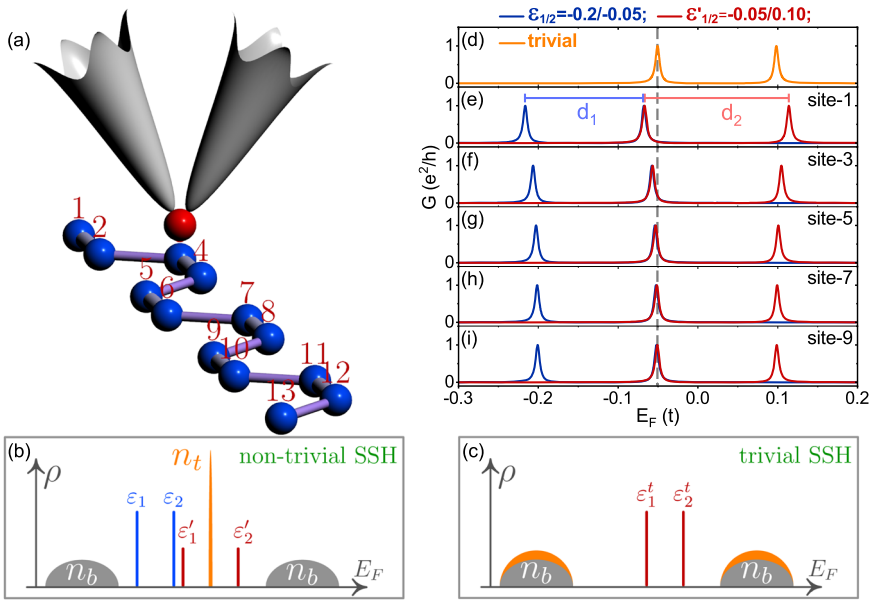

Fig. 1 The schematic setup and related measurement features of TFC in SSH model. a Schematic plot of the transport device measuring the TFC in the SSH chain. **b**, **c** Band structure for non-trivial/trivial SSH model and the QD levels. The number of electron of the zero mode n_t in **b** is the same as the increased portion of the bulk states' number of electron in **c**, as denoted by the orange areas. **d**–**i** Fermi level dependence of the conductance curves for **d** trivial end of the SSH chain with $t_1 = 0.6t$, and $t_2 = 0.37t$; and **e**–**i** non-trivial end of the same SSH chain with $t_1 = 0.37t$, and $t_2 = 0.6t$. The parameters are drawn from a practical experiment where the SSH chain is built from the graphene naoribbon[37] and $t = 1eV$ is used as the energy unit. Other parameters are $U = 0.05t$, $t_k = 0.1t$, $t_c = 0.01t$.

RESULTS

Model

Our transport system measuring TFC is shown in Fig. 1a that a QD (the red ball) with two energy levels is connected to two separated terminals (the grey ones). The QD can be moved to the vicinity of the target atom of the topological system (e.g. a SSH chain shown by blue balls) and weakly bonds to it, leading to a Coulomb interaction[39–42]. In this way, the charge possessed by the target atom can be extracted from the shift of the differential conductance resonance peak[43–45]. Then the amount and spatial distribution of the TFC possessed by the topological edge states can be extracted by measuring all the atoms involved.

There are two basic rules for this TFC measurement scheme: (i) Any topological edge state carries an integer number of electrons. (ii) A trivial insulator is charge neutral when the Fermi energy lies inside the gap. The first rule enables us to determine the Coulomb interaction strength, while the second rule enables us to count the charge by comparing the charge difference between a trivial insulator and its non-trivial counterpart. Remarkably, in the presence of disorder, whether the second rule is still valid depends on the symmetry of the disorder term and the dimension of the topological material.

We first apply our method to the SSH chain composed of an odd number of sites, in which the TFC is presented only in one end of the chain (non-trivial end), while another end of this chain (trivial end) behaves like a trivial insulator. In this way, the measurement and the charge difference comparison can be conducted in a single device. The total Hamiltonian of the system is in the form of:

$$H = H_{\mathrm{QD}} + H_{\mathrm{SSH}} + H_{\mathrm{c}}, \tag{1}$$

where the two-level QD (with level index i) is connected to the source and drain (with index $a = L, R$) as $H_{\mathrm{QD}} = \sum_{ka}\varepsilon_{ka}C^{\dagger}_{ka}C_{ka} + \sum_i \varepsilon_i a^{\dagger}_i a_i + \sum_{ka,i} t_k (C^{\dagger}_{ka}a_i + h.c.)$ with $C^{\dagger}_{ka}$ and $a^{\dagger}_i$ the creation operators in terminals and QD, respectively. Here ε_i is the *i-th* energy level for the QD and t_k is the coupling between terminals and the QD. $H_{\mathrm{SSH}} = \sum_n (t_1 b^{\dagger}_{2n-1} b_{2n} + t_2 b^{\dagger}_{2n+1} b_{2n} + h.c.)$ describes the SSH chain and $t_{1/2}$ is the alternative coupling between nearest sites. The coupling term reads $H_c = \sum_i [U a^{\dagger}_i a_i b^{\dagger}_s b_s + t_c (a^{\dagger}_i b_s + b^{\dagger}_s a_i)]$ with U the Coulomb interaction strength, and t_c the direct tunneling between the QD and the target site (denoted by index s) of the SSH chain.

In the calculation, the on-site energy of the QD and its Coulomb interaction to the target site constitute the unperturbed Hamiltonian H_0 (3×3 matrix in the basis of $\{a_1, a_2, b_s\}$). The rest part of H [see Eq. (1)] is regarded as perturbations (see Methods section). In this way, the differential conductance of the system is obtained from the Green's function[46,47]

$$\mathcal{G}(E_F) = \frac{e^2}{h}\mathrm{Tr}[\Gamma^r_L G^r \Gamma^r_R (G^r)^{\dagger}]. \tag{2}$$

Here $\Gamma^r_{L/R}$ is the symmetric line-width function of the terminals and G^r is the retarded Green's function. The unperturbed retarded Green's function for the *n-th* level in QDs from H_0 reads: $g^r_n(E) = 1/(E - \varepsilon_n - U\langle n_s\rangle + i\eta)$ with η a positive infinitesimal and $\langle n_s\rangle$ the total electron number below the Fermi level. G^r is numerically obtained from the Dyson equation for g^r and they share similar features. When the QD is weakly coupled to the topological system, the resonance peaks of the $\mathcal{G}(E_F)$ shift from ε_i to $\varepsilon_i + U\langle n_s\rangle$ due to the Coulomb blockade[48,49]. The weak coupling assumption is quite reasonable since the direct tunneling t_c exponentially decays with the distance while the Coulomb interaction U is inversely proportional to the distance. In practice, U is a priorly unknown parameter which should also be extracted from the measurement.

Measurement of e/2 charge in SSH models

For a QD consisting of two energy levels $\varepsilon_1, \varepsilon_2$, when both these two levels are below the fractionally-charged subgap zero mode of the SSH chain as $\varepsilon_1 < \varepsilon_2 < 0$ [Fig. 1b], the corresponding conductance peaks are separated by $d_1 = \varepsilon_2 - \varepsilon_1$. Alternatively, by tuning the gate voltage V_g, these two levels can be elevated to ε'_1 and ε'_2 that $\varepsilon'_1 < 0$ and $\varepsilon'_2 > 0$ [Fig. 1b]. Since $\varepsilon'_1 = \varepsilon_1 + eV_g$ and

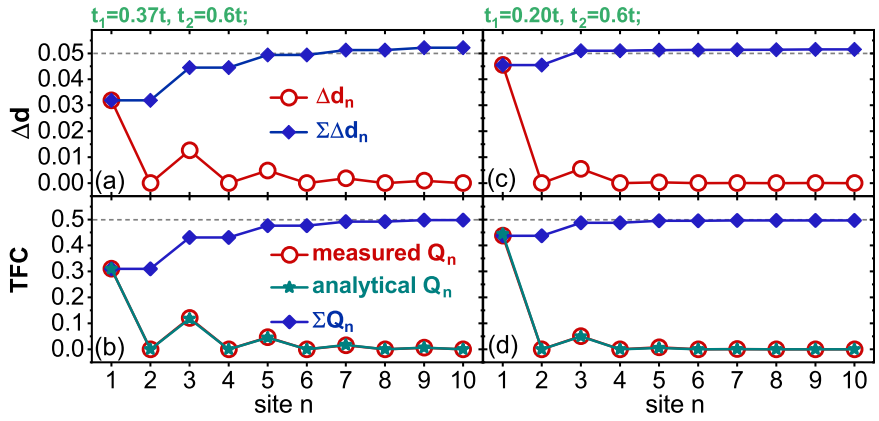

Fig. 2 The TFC and its distribution in the SSH chain. a, **c** The shift of the conductance peaks' separation $\Delta d_n = d_2 - d_1$ [drawn from Fig. 1e–i] and its summation $\Sigma_n \Delta d_n$. **b**, **d** The TFC distribution Q_n and its summation $\Sigma_n Q_n$.

$\varepsilon_2' = \varepsilon_2 + eV_g + Un_t$, where n_t denotes the amount of charge of the zero mode at the site being measured, now the conductance peaks are separated as $d_2 = \varepsilon_2' - \varepsilon_1' = d_1 + Un_t$. Thus, at this specific site, $d_2 - d_1 = Un_t$, which measures the product of U and n_t. Owing to the integer charge rule mentioned earlier ($\Sigma n_t = 1$), when all the sites that the TFC resides in are considered, we have $\Sigma(d_2 - d_1) = U \Sigma n_t = U$ and consequently, the value of U is measured.

Figure 1e–i display the $\mathcal{G} - E_F$ relations for all the odd sites at the non-trivial end of the SSH chain for both (i) $\varepsilon_1, \varepsilon_2 < 0$; and (ii) $\varepsilon_1' < 0, \varepsilon_2' > 0$. The conductance peak shifts for even sites are trivial as $d_1 = d_2$ (see Supplementary Fig. 3). Figure 2a summarizes the site n dependence of $\Delta d_n = d_2 - d_1$ extracted from Fig. 1e–i. For odd sites, Δd_n decreases as the target site moves from the end to the bulk, and for all the even sites, $\Delta d_n = 0$. Summing them up gives $U_0 = \Sigma \Delta d_n = 0.052t$, which is quite close to the input value of $U = 0.05t$ and demonstrates that the priorly unknown parameter U_0 can be obtained from the transport measurement. The small difference between U_0 and U may come from three issues. (i) Small but non-zero direct tunnelings ($t_c = 0.01t$, compared with $t_k = 0.1t$) shifting the $\mathcal{G}$ peak position; (ii) Peak's position of $\mathcal{G}$ is obtained via numerical treatment other than exact analytical derivation; and iii) $\mathcal{G}$ is obtained by iteration with a finite but accepatable accuracy.

To figure out the amount and the distribution of the TFC, we need to measure the trivial end of the same SSH chain while keeping V_g unchanged. Compared with the non-trivial end, the bulk states' charge amount in the trivial end is increased by n_t [see Fig. 1c]. The conductance peaks now locate at ε_1^t and ε_2^t, where $\varepsilon_1^t = \varepsilon_1' - U_0 Q_n / e$ and Q_n is the TFC at site n. Therefore, Q_n can be extracted from the conductance peak shift as $Q_n = (\varepsilon_1' - \varepsilon_1^t) e / U_0$ since U_0 has been obtained previously. Note that Q_n is independent of U. Thus, the obtained Q_n is still correct even if there is a screening effect which only renormalizes the value of U.

Figure 2c displays the spatial distribution of Q_n and its summation $\Sigma_n Q_n$. Such a summation is truncated when Δd_n decays into a sufficiently small value. For odd sites, Q_n decreases as the target site moves from the end to the bulk of the SSH chain and for even sites, Q_n is nearly zero. These are in good agreement with the analytical result: $Q_n = (e/2)(t_1/t_2)^{n-1}[1 - (t_1/t_2)^2]$ for the odd site, and $Q_n = 0$ for the even site[50,51]. For the present SSH chain model with parameters adopted from experiment[37], 10 sites are sufficient for the truncation in summation. In Fig. 2b $\Sigma_n Q_n$ approaches $e/2$, confirming the 1/2 charge quantization of the TFC in the clean SSH model. Figure 2c, d displays the TFC obtained from the above scheme for another set of parameters $t_1 = 0.2t$ and $t_2 = 0.6t$ (see Supplementary Fig. 3). In such a case, $U_0 = 0.052t$ [Fig. 2c] can be drawn from the transport data. The measurement scheme also shows that the TFC now becomes more localized at the end of the SSH chain, while the TFC amount is still close to $e/2$ [Fig. 2d]. All these are in perfect match with the analytical results[50,51]. Such transport measurement scheme is also adopted for obtaining the spatial distribution and verifying the $e/2$ amount of the TFC carried by the topological corner state of the quadrupole insulator[11,12], where the latter is regarded as the two-dimensional analogy of the SSH chain (see Supplementary Note 6).

Though the measurement scheme above is based on a comparison between trivial and non-trivial SSH chain, it also works for the SSH chain with only non-trivial end states. This is because the electron density distribution in the sites far away from the end of the SSH chain is the same for both non-trivial and trivial SSH chain. Hence the sites far away from the bulk of the non-trivial SSH chain can be treated as a trivial SSH chain end because of the translational invariance. So far, there being just only a single value of U is required in our proposal. For another SSH-type model in which each site supports two orbitals so that there are two different U's[52], the current version of our measurement scheme will not work well. Nevertheless, when the separation between the QD and the target atom is large compared to the lattice constant of the SSH chain, our treatment is a good approximation and the amount of TFC can still be obtained (see Supplementary Note 5).

The influence of disorder effects

Disorder effect including bond disorder and Anderson disorder is widely presented in practical experiments, which may induce charge fluctuation and thus hinder the identification of the genuine fractional charge. The bond disorder, for instance, in the form of $\sum_i w_i (b_i^\dagger b_{i+1} + h.c.)$ in the SSH model where w_i is uniformly distributed as $w_i \in [-W/2, W/2]$ and W is the disorder strength[53], preserves the chiral symmetry obeyed by the clean SSH model. Hence the charge neutral rule for the trivial insulator remains valid, and the fluctuation only comes from the redistribution of the TFC in the non-trivial state. As shown in Fig. 3b, under bond disorder, although the distribution of the TFC deviates from the clean SSH model, the TFC amount still approaches $e/2$.

In contrast, the Anderson disorder $\sum_i w_i b_i^\dagger b_i$[54] in the SSH model breaks the chiral symmetry so that the charge neutral rule is only satisfied in an average manner. The TFC fluctuation is now ascribed to the redistribution of the electron density of both the

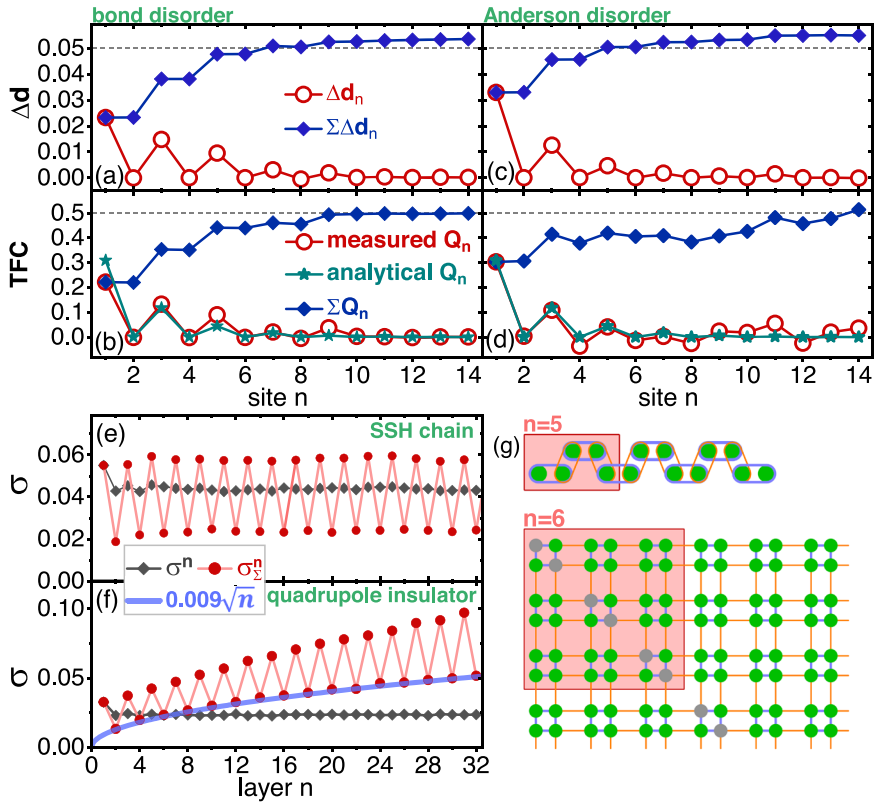

Fig. 3 Features of TFC under disorders. a–d The TFC distribution in the disordered SSH model as **a**, **b** bond disorder with $W = 0.2t$; **c**, **d** Anderson disorder with $W = 0.2t$. All other parameters are the same as those in Fig. 1. **e**, **f** Standard deviation of the TFC σ^n at site n, and standard deviation of the total TFC inside the area concerned σ^n_Σ under Anderson disorder for **e** SSH chain, and **f** quadrupole insulator. These two models are sketched in **g**, where the red rectangles indicate the area being concerned. Both these two models have the same band gap (~0.4t), sample length and disorder strength $W = 0.5t$. In **e**, **f**, the standard deviations are drawn from 10^4 disordered configurations.

bulk states (in the trivial and non-trivial SSH chain) and the topological edge state (in the non-trivial SSH chain). The transport data confirms that the position of the conductance peaks in each site of the trivial SSH chain also fluctuates under Anderson disorder (see Supplementary Fig. 3), which is in stark contrast to the bond disorder condition. As a result, though the amount of the TFC is approximately $e/2$, both the TFC distribution Q_n and its summation $\sum_n Q_n$ shows significant fluctuation [Fig. 3d] even for the sites far away from the end of the SSH chain.

A question then arises that whether the fluctuation of the total TFC becomes more significant if more sites are taken into consideration. This issue is essential because in higher-dimensional systems, the site number involved for the topological edge state is proportional to the power of the localization length of the edge state. For the one-dimensional SSH chain, the standard deviation of the TFC at each site $\sigma^n \equiv \sigma(Q_n)$ and the standard deviation of the total TFC inside the area concerned $\sigma^n_\Sigma \equiv \sigma(\sum_{i\in\square} Q_i)$ is investigated ["□" indicates the area concerned, shown by the red rectangles in Fig. 3g]. Significantly, both σ^n and σ^n_Σ are in the same order for the one-dimensional SSH chain [Fig. 3e]. As a comparison, as shown in Fig. 3f, g, for an Anderson-disordered two-dimensional quadrupole insulator[11,12] whose band gap and disorder strength are both the same as the one-dimensional SSH chain, although σ^n is nearly independent of n [n refers the index of the grey dots in Fig. 3g], σ^n_Σ quickly increases in the fashion proportional to $\sqrt{n}$. Such fluctuation behavior is certainly detrimental to the TFC measurement.

In case of Anderson disorder, the fluctuations of Q_n in adjacent sites are correlated so that the fluctuation of the total TFC σ^n_Σ inside the area concerned is only determined by the charge fluctuation at the boundaries. For one-dimensional model like SSH chain, such a boundary is a single site, while for higher-dimensional systems like quadrupole insulator, the number of sites at the boundary increases with the area being concerned. Consequently, σ^n_Σ does not increase with n for one-dimensional topological system, while it quickly increases with n for higher-dimensional system. In other words, for higher-dimensional topological materials supporting TFC, the disorder-induced fluctuation of the TFC is reduced for a better-localized topological edge state. The results of dimension and disorder effects on TFC measurement are universal. They hold true not only for topological electronic systems, but also for topological classic wave systems. For classic wave systems, the TFC is measured via integrating the local density of states[32–34]. Though the experiments have shown specific spatial crystal symmetries related to the TFC are broken by the inevitable disorder effect, the TFC could still be observed since the topological corner states here are well localized.

Measurement of 2e/3 charge in breathing kagome lattice

Recently, a TFC of $2e/3$ is reported in breathing kagome lattice[14–17], though such material is two-dimensional, the topological corner states therein can be well localized (e.g. monolayer MoS_2[16,17]), so that our transport measurement scheme is still applicable. It is worth noting that in addition to the topological corner state, the zigzag-edged breathing kagome lattice also possesses a metallic one-dimensional edge state, hence the TFC here can not be detected by our scheme. Therefore, we first turn

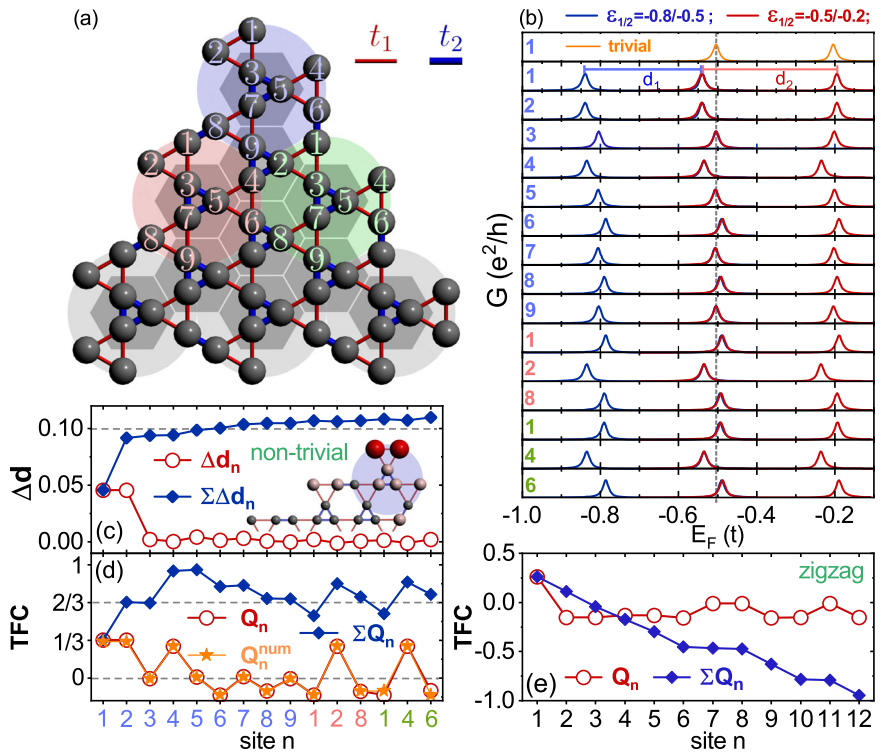

Fig. 4 TFC in breathing kagome models. a Schematic plot of the armchair-edged breathing kagome lattice that the red (blue) bond indicates hopping amplitude t_1 (t_2). The sites are numbered in each individual supercell as highlighted by colored disks. **b** The conductance curves in each site for both the trivial ($t_1 = t, t_2 = 0.3t$) and the non-trivial ($t_1 = 0.3t, t_2 = t$) cases. **c** The conductance peak shift Δd_n drawn from **b**. Inset: the TFC is mainly distributed at the two sites marked by the red balls. **d** The TFC distribution Q_n and $\Sigma_n Q_n$ drawn from **c**, where the colored numbers in the horizontal axis refer to the site indices in **a**. **e** The same TFC distribution for zigzag-edged breathing kagome model. Other parameters are $U = 0.1t$, $t_k = 0.1t$, and $t_c = 0.01t$.

to investigate the armchair-edged breathing kagome lattice whose one-dimensional edge state is insulating.

Figure 4a shows a corner of a triangular armchair-edged breathing kagome lattice that the three supercells near the corner being mainly concerned are highlighted by colored disks. Figure 4b exhibits the conductance curves obtained from our measurement scheme for the representative 15 of the 27 sites inside these three supercells. The conductance peak shifts Δd_n are listed in Fig. 4c, and the TFC Q_n as well as its summation are shown in Fig. 4d. The Q_n obtained is in good agreement with the numerical result Q_n^{num} from the diagonalization treatment[55]. It is shown that the TFC is mainly distributed in the corner sites [see inset of Fig. 4c]. At the edge, for example, sites 1, 2, and 8 in the pale red supercell contributes nearly zero net charge after summation. Finally, a quantized $2e/3$ TFC is obtained as expected.

As a comparison [see Fig. 4e], we also show that our transport measurement scheme fails to determine the TFC in the zigzag-edged breathing kagome lattice[14], because the "charge neutral" rule, one of the two basic rules of our measurement scheme, is broken by its metallic one-dimensional topological edge state[17] (see Supplementary Fig. 7). Finally, it is worth noting that the spin degeneracy has been ignored from the beginning. When the spin doubling is also taken into consideration, for instance, for the quadrupole insulator, one may be confused by the "integer" TFC of $2(e/2)$[29]. In contrast, the $2e/3$ TFC is always fractional even after considering the spin doubling, which serves as an additional advantage for the breathing kagome materials.

DISCUSSION

We have presented the measurement scheme as well as the suitable materials. Now we turn to discuss feasible platforms supporting the measurement circuit, as well as the possible materials supporting TFC. In some pioneering experimental works, a superconducting quantum interference device on a tip (SOT) is used to study the spatial distribution of topological states and heat generation[56–58]. The SOT, serving as an mobile nanocircuit, moves precisely in a controlled manner that the separation between the tip and the sample can keep constant. Modified tips with a single molecule or specific clusters in scanning tunnelling microscopy were achieved in past years[59,60]. By attaching the SOT with a QD (a molecule or a cluster), it forms a moveable QD and it does not need to work below the superconducting critical temperature. Such a proposed measurement apparatus can be used in a graphene-nanoribbon-based SSH model to study the fractional charge[36,37]. Alternatively, in experiment a series of QDs has been fabricated in two-dimensional electron gas[61]. It can also be used for building suitable samples supporting TFC by tuning the gate voltages properly (see Supplementary Note 8).

In summary, a transport measurement scheme is proposed to measure the amount and the spatial distribution of TFC in topological materials. Through such a scheme, the $e/2$ amount of the TFC in the SSH model as well as its spatial distribution has been verified. The bond disorder preserving chiral symmetry will only slightly modify the spatial profile of the TFC. It implies that seeking a material in which the symmetry related to the TFC is quite robust will facilitate the experimental identification of the quantized TFC. In the presence of Anderson disorder breaking chiral symmetry, the fluctuation of the TFC amount is largely suppressed in one-dimensional systems. Meanwhile, for Anderson-disordered higher-dimensional topological materials such as breathing kagome lattice, the amount and the distribution of the TFC can still be obtained for the well-localized topological corner states. It indicates that in specific condensed matter materials, the difficulty of experimentally

distinguishing the genuine fractional charge and the disorder-induced fluctuation can be circumvented.

METHODS

The solving of the retarded Green's function

The retarded Green's function $G^r(E_F)$ needs to be solved by iteration for non-zero U[62]

$$\mathbf{G^r}(E) = \left[E - \begin{pmatrix} \varepsilon_1 + Un_s & 0 & 0 \\ 0 & \varepsilon_2 + Un_s & 0 \\ 0 & 0 & U(n_1+n_2) \end{pmatrix} - \mathbf{\Sigma}^r \right]^{-1} \tag{3}$$

with $\mathbf{\Sigma}^r$ the retarded self-energy and the matrix $\mathbf{G^r}(E)$ is in the basis $\{a_1, a_2, b_s\}$. The particle numbers $n_{1,2,s}$ in equation (3) refers to electron number in the QD level ε_1, ε_2 and in the target site s, respectively. They are obtained through solving the integral equation self-consistently by iteration, e.g. $n_s = -\frac{1}{\pi}\int_{-\infty}^{E_F} \mathrm{Im}[\mathbf{G^r}_{(3,3)}(E)]dE$.

Numerical solution for TFC

In Figs. 3e, f and 4c, TFC is obtained via the tight-binding models of finite-size samples. Solving the eigen-equations $H\Psi_i = E_i\Psi_i$, the total charge $\mathcal{Q}_n = e\sum_{i\in occ}|\Psi_i(n)|^2$ is obtained by summing up the states below the Fermi level of site n. The net charge is obtained by $Q_n = Q_0 - \mathcal{Q}_n$ with Q_0 the charge of the nucleus. In a clean trivial insulating system, $Q_n = 0$ for all sites due to the charge neutral condition.

DATA AVAILABILITY

The data that support the findings of this study are available from the corresponding author upon reasonable request.

Received: 16 November 2022; Accepted: 9 May 2023;
Published online: 01 June 2023

REFERENCES

1. Tsui, D. C., Stormer, H. L. & Gossard, A. C. Two-dimensional magnetotransport in the extreme quantum limit. *Phys. Rev. Lett.* **48**, 1559 (1982).
2. Laughlin, R. B. Anomalous quantum Hall effect: an incompressible quantum fluid with fractionally charged excitations. *Phys. Rev. Lett.* **50**, 1395 (1983).
3. Laughlin, R. B. Nobel lecture: fractional quantization. *Rev. Mod. Phys.* **71**, 863 (1998).
4. Arovas, D., Schrieffer, J. R. & Wilczek, F. Fractional statistics and the quantum Hall effect. *Phys. Rev. Lett.* **53**, 722 (1984).
5. Jackie, R. & Rebbi, C. Solitons with fermion number 1/2. *Phys. Rev. B* **13**, 3398 (1976).
6. Su, W. P., Schrieffer, J. R. & Heeger, A. J. Soliton excitations in polyacetylene. *Phys. Rev. B* **22**, 2099 (1980).
7. Su, W. P., Schrieffer, J. R. & Heeger, A. J. Solitons in polyacetylene. *Phys. Rev. Lett.* **42**, 1698 (1979).
8. Goldstone, J. & Wilczek, F. Fractional quantum numbers on solitons. *Phys. Rev. Lett.* **47**, 986 (1981).
9. Kivelson, S. & Schrieffer, J. R. Fractional charge, a sharp quantum observable. *Phys. Rev. B* **25**, 6447 (1982).
10. Li, T. H., Zhu, P. H., Benalcazar, W. A. & Hughes, T. L. Fractional disclination charge in two-dimensional Cn-symmetric topological crystalline insulators. *Phys. Rev. B* **101**, 115115 (2020).
11. Benalcazar, W. A., Bernevig, B. A. & Hughes, T. L. Quantized electric multipole insulators. *Science* **357**, 61 (2017).
12. Benalcazar, W. A., Bernevig, B. A. & Hughes, T. L. Electric multipole moments, topological multipole moment pumping, and chiral hinge states in crystalline insulators. *Phys. Rev. B* **96**, 245115 (2017).
13. Lemut, G., Mierzejewski, M. & Bonča, J. Complete Many-Body Localization in the t-j model caused by a random magnetic field. *Phys. Rev. Lett.* **119**, 246601 (2017).
14. Ezawa, M. Higher-order topological insulators and semimetals on the breathing kagome and pyrochlore lattices. *Phys. Rev. Lett.* **120**, 026801 (2018).
15. van Miert, G. & Ortix, C. On the topological immunity of corner states in two-dimensional crystalline insulators. *npj Quantum Mater.* **5**, 63 (2020).
16. Zeng, J., Liu, H. W., Jiang, H., Sun, Q. F. & Xie, X. C. Multiorbital model reveals a second-order topological insulator in 1H transition metal dichalcogenides. *Phys. Rev. B* **104**, L161108 (2021).
17. Qian, S. F., Liu, G. B., Liu, C. C. & Yao, Y. G. Cn-symmetric higher-order topological crystalline insulators in atomically thin transition metal dichalcogenides. *Phys. Rev. B* **105**, 045417 (2022).
18. Moore, G. & Read, N. New method for high-accuracy determination of the fine-structure constant based on quantized Hall resistance. *Nucl. Phys. B* **360**, 362 (1991).
19. Ivanov, D. A. Non-Abelian statistics of half-quantum vortices in *p*-wave superconductors. *Phys. Rev. Lett.* **86**, 268 (2001).
20. Wilczek, F. Magnetic flux, angular momentum, and statistics. *Phys. Rev. Lett.* **48**, 1144 (1982).
21. Nayak, C., Simon, S. H., Stern, A., Freedman, M. & Das Sarma, S. Non-Abelian anyons and topological quantum computation. *Rev. Mod. Phys.* **80**, 1083 (2008).
22. Wu, Y. J., Liu, H. W., Liu, J., Jiang, H. & Xie, X. C. Double-frequency Aharonov-Bohm effect and non-Abelian braiding properties of Jackiw-Rebbi zero-mode. *Natl Sci. Rev.* **7**, 572 (2020).
23. Wu, Y. J., Jiang, H., Liu, J., Liu, H. W. & Xie, X. C. Non-Abelian braiding of Dirac Fermionic modes using topological corner states in higher-order topological insulator. *Phys. Rev. Lett.* **125**, 036801 (2020).
24. Tan, Y., Huang, Z. H. & Liu, X.-J. Two-particle Berry phase mechanism for Dirac and Majorana Kramers pairs of corner modes. *Phys. Rev. B* **105**, L041105 (2022).
25. Boross, P. K., Asbóth, J., Széchenyi, G., Oroszlány, L. & Pályi, A. Poor man's topological quantum gate based on the Su-Schrieffer-Heeger model. *Phys. Rev. B* **100**, 045414 (2019).
26. Fu, B., Zou, J. Y., Hu, Z., Wang, H. W. & Shen, S. Q. Quantum anomalous semimetals. *npj Quantum Mater.* **7**, 94 (2022).
27. de-Picciotto, R. et al. Direct observation of a fractional charge. *Nature* **389**, 162 (1997).
28. Saminadayar, L., Glattli, D. C., Jin, Y. & Etienne, B. Observation of the e/3 fractionally charged Laughlin quasiparticle. *Phys. Rev. Lett.* **79**, 2526 (1997).
29. Ortix, C. Electrons broken into pieces at crystal defects. *Nature* **589**, 356 (2021).
30. Rainis, D., Saha, A., Klinovaja, J., Trifunovic, L. & Loss, D. Transport signatures of fractional Fermions in Rashba nanowires. *Phys. Rev. Lett.* **112**, 196803 (2014).
31. Qi, X.-L., Hughes, T. L. & Zhang, S.-C. Fractional charge and quantized current in the quantum spin Hall state. *Nat. Phys.* **4**, 273 (2008).
32. Peterson, C. W. et al. A fractional corner anomaly reveals higher-order topology. *Science* **368**, 1114 (2020).
33. Peterson, C. W. et al. Trapped fractional charges at bulk defects in topological insulators. *Nature* **589**, 376 (2021).
34. Liu, Y. et al. Bulk-disclination correspondence in topological crystalline insulators. *Nature* **589**, 381 (2021).
35. Franke, K. J. & Von Oppen, F. Designer topology in graphene nanoribbons. *Nature* **560**, 175 (2018).
36. Rizzo, D. J. et al. Topological band engineering of graphene nanoribbons. *Nature* **560**, 204 (2018).
37. Gröning, O. et al. Engineering of robust topological quantum phases in graphene nanoribbons. *Nature* **560**, 209 (2018).
38. Zhu, Z. et al. A tunable and unidirectional one-dimensional electronic system $Nb_{2n+1}Si_nTe_{4n+2}$. *npj Quantum Mater.* **5**, 35 (2020).
39. Johnson, A. C., Marcus, C. M., Hanson, M. P. & Gossard, A. C. Coulomb-modified Fano resonance in a one-Lead quantum dot. *Phys. Rev. Lett.* **93**, 106803 (2004).
40. Beenakker, C. W. J. Theory of Coulomb-blockade oscillations in the conductance of a quantum dot. *Phys. Rev. B* **44**, 1646 (1991).
41. Groshev, A. Coulomb blockade of resonant tunneling. *Phys. Rev. B* **42**, 5895 (1990).
42. Baines, D. Y. et al. Transport through side-coupled double quantum dots: From weak to strong interdot coupling. *Phys. Rev. B* **85**, 195117 (2012).
43. Berkovits, R., von Oppen, F. & Gefen, Y. Theory of charge sensing in quantum-dot structures. *Phys. Rev. Lett.* **94**, 076802 (2005).
44. Kano, S., Tada, T. & Majima, Y. Nanoparticle characterization based on STM and STS. *Chem. Soc. Rev.* **43**, 3957 (2014).
45. Chiang, C. L., Xu, C., Han, Z. & Ho, W. Real-space imaging of molecular structure and chemical bonding by single-molecule inelastic tunneling probe. *Science* **344**, 885 (2014).
46. Güclü, A. D., Sun, Q. F. & Guo, H. Kondo resonance in a quantum dot molecule. *Phys. Rev. B* **68**, 245323 (2003).
47. Sun, Q. F., Xing, Y. X. & Shen, S. Q. Double quantum dot as detector of spin bias. *Phys. Rev. B* **77**, 195313 (2008).

48. Liu, J., Sun, Q. F. & Xie, X. C. Enhancement of the thermoelectric figure of merit in a quantum dot due to the Coulomb blockade effect. *Phys. Rev. B* **81**, 245323 (2010).
49. Haug, H. & Jauho, A. P., Quantum kinetics in transport and optics of semiconductors (Springer-Verlag, Berlin, 1998).
50. Peng, Y., Bao, Y. M. & von Oppen, F. Boundary Green functions of topological insulators and superconductors. *Phys. Rev. B* **95**, 235143 (2017).
51. Meier, E. J., Alex, An,F. & Gadway, B. Observation of the topological soliton state in the Su-Schrieffer-Heeger model. *Nat. Commun.* **7**, 13986 (2016).
52. Nelson, A., Neupert, T., Bzdušek, T. & Alexandradinata, A. Multicellularity of delicate topological insulators. *Phys. Rev. Lett.* **126**, 216404 (2021).
53. Song, J. T. et al. Dependence of topological Anderson insulator on the type of disorder. *Phys. Rev. B* **85**, 195125 (2012).
54. Qiao, Z. H., Jung, J., Niu, Q. & MacDonald, A. H. Electronic highways in bilayer graphene. *Nano Lett.* **11**, 3453 (2011).
55. Zhang, Z. Q., Wu, B. L., Chen, C. Z. & Jiang, H. Global phase diagram of disordered higher-order Weyl semimetals. *Phys. Rev. B* **104**, 014203 (2021).
56. Vasyukov, D. et al. A scanning superconducting quantum interference device with single electron spin sensitivity. *Nat. Nanotechnol.* **8**, 639 (2013).
57. Marguerite, A. et al. Imaging work and dissipation in the quantum Hall state in graphene. *Nature* **575**, 628 (2019).
58. Aharon-Steinberg, A. et al. Long-range nontopological edge currents in charge-neutral graphene nature. *Nature* **593**, 528 (2021).
59. Cheng, Z. et al. Direct imaging of molecular orbitals of metal phthalocyanines on metal surfaces with an O_2-functionalized tip of a scanning tunneling microscope. *Nano Res.* **4**, 523 (2011).
60. Bian, K. et al. Scanning probe microscopy. *Nat. Rev. Methods Prim.* **1**, 36 (2021).
61. Volk, C. et al. Loading a quantum-dot based "Qubyte" register. *npj Quantum Inf.* **5**, 29 (2019).
62. Sun, Q. F. & Guo, H. Kondo resonance in a multiprobe quantum dot. *Phys. Rev. B* **64**, 153306 (2001).

ACKNOWLEDGEMENTS

We thank Z.J., L.H.W., and Z.Z.Q. for fruitful discussions. This work is financially supported by the National Basic Research Program of China (Grants Nos. 2019YFA0308403 and 2022YFA1403700), the National Natural Science Foundation of China (Grant Nos. 11874298 and 11822407), the Strategic Priority Research Program of Chinese Academy of Sciences (Grant No. XDB28000000), China Postdoctoral Science Foundation (Grant No. 2021M690233), and Natural Science Basic Research Plan in Shaanxi Province of China (Grant No. 2019JM-187).

AUTHOR CONTRIBUTIONS

H.J. initiated the idea from discussions with Y.J.W., and X.C.X. C.S.G. performed the calculation with the suggestions from Q.F.S. and Y.J.W., H.J. and X.C.X. supervised the project. All authors were involved in analyzing the data and writing the manuscript.

COMPETING INTERESTS

The authors declare no competing interests.

ADDITIONAL INFORMATION

Supplementary information The online version contains supplementary material available at https://doi.org/10.1038/s41535-023-00558-7.

Correspondence and requests for materials should be addressed to Hua Jiang.

Reprints and permission information is available at http://www.nature.com/reprints

Publisher's note Springer Nature remains neutral with regard to jurisdictional claims in published maps and institutional affiliations.